Chemical Science

Accepted Manuscript

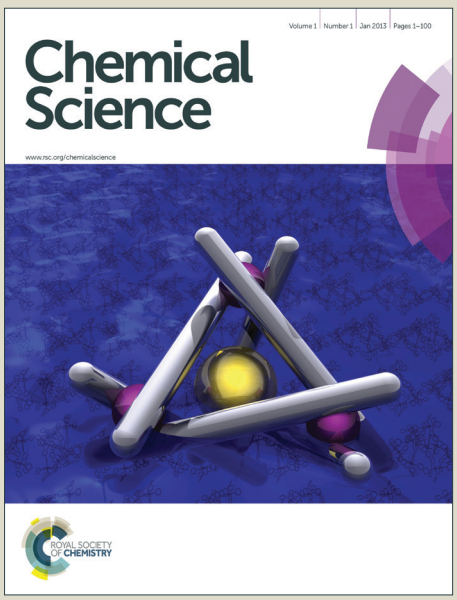

ROYAL SOCIETY OF CHEMISTRY

www.rsc.org/chemicalscience

Chemical Science

RSCPublishing

ARTICLE

Revisiting the nature of Cu-sites in activated Cu-SSZ-13 catalyst for SCR reaction

Cite this: DOI: 10.1039/x0xx00000x

E. Borfecchia,[a,b] K. A. Lomachenko,[a,e] F. Giordanino,[a,b] H. Falsig,[c] P. Beato,[c] A. V. Soldatov,[e] S. Bordiga,[a,b] C. Lamberti,* [a,d,e]

Received ooth January 2012,
Accepted ooth January 2012

DOI: 10.1039/x0xx00000x

www.rsc.org/

Cu-SSZ-13 is a highly active NH_3-SCR catalyst for the abatement of harmful nitrogen oxides (NO_x, x = 1, 2) from the exhaust of lean-burn engines. The study of Cu-speciation occurring upon thermal dehydration is a key step for the understanding of the enhanced catalytic properties of this material and for identifying the SCR active sites and their redox capability. Herein, we combined FTIR, X-ray absorption (XAS) and emission (XES) spectroscopies with DFT computational analysis to elucidate the nature and location of the most abundant Cu-sites in the activated catalyst. Different Cu species have been found to be dominant as a function of the dehydration temperature and conditions. Data analysis revealed that the dehydration process of Cu cations is essentially completed at 250 °C, with the formation of dehydrated $[CuOH]^+$ species hosted in a close proximity of 1 Al sites in both *d6r* and *8r* units of the SSZ-13 matrix. These species persist at higher temperature only if a certain amount of O_2 is present in the gas feed, while in inert conditions they undergo virtually total "self-reduction" as a consequence of an OH extra-ligand loss, resulting in bi-coordinated bare Cu^+ cations. Synchrotron characterization supported by computational analysis allowed a unprecedented quantitative refinement of local environment and structural parameters of these Cu(II) and Cu(I) species.

Introduction

Selective catalytic reduction by NH_3 (NH_3-SCR) is considered to be one of the most efficient ways to remove environmentally harmful nitrogen oxides (NO_x, x = 1, 2) from the exhaust of lean-burn engines.[1-4] A variety of Cu-substituted zeolites have been investigated for NH_3-SCR activity, and their stability in catalyst operating conditions has been examined. Early development efforts were focused on Cu-ZSM-5 and Cu-beta catalysts for their high activity over a wide range of conditions.[5, 6] Most recently, small pore CHA-based material, *i.e.* Cu-exchanged SSZ-13, has become the subject of considerable study as it is now used commercially.[4, 7-11] Compared to Cu-ZSM-5 and Cu-beta, Cu-SSZ-13 has been found to be more active and selective, and less prone to deactivation by hydrocarbon inhibition or thermal degradation.[12] Knowledge of the location and coordination of copper in the SSZ-13 zeolite is fundamental for fully understanding its superior SCR performances and for the clarification of the active species involved in the reaction mechanism.

SSZ-13 is a three-dimensional zeolite made up of double six rings (*d6r*), which are connected by four member ring units, and by 8-membered *cha* composite units (*8r*). In literature, most of the works agree with the fact that Cu-SSZ-13 mainly contains monomeric Cu species which have been proposed to be the active sites for NO_x reduction with NH_3.[3] Lobo and coworkers[13] were the first to perform a XRD study on a O_2-activated Cu-SSZ-13 catalyst (Si/Al = 6 and Cu/Al = 0.35), suggesting that Cu is only present as isolated Cu^{2+} ions, exclusively located in 6-membered ring windows, with a coordination number of 3 and average Cu–O distances of 2.2 − 2.3 Å. Korhonen *et al.*[14] employed UV-Vis and EXAFS spectroscopy, supporting the location of Cu^{2+} ions on the plane of the *d6r* sub-units as dominant species in a O_2-activated Cu-SSZ-13 sample (Si/Al = 9 and Cu/Al = 0.18). They proposed that, after calcination, three framework oxygens coordinate to Cu^{2+} ions at an average distance of 1.93 Å.

Later, on the basis of TPR and FTIR results, Kwak *et al.*[10] observed another Cu ion location in SSZ-13 (Si/Al = 6) for Cu/Al > 0.2, which they assigned to isolated Cu^{2+} ions in the *8r*. Subsequently, Gao *et al.*[11] concluded that for 0.2 ≤ Cu/Al ≤ 0.4 the active sites for ammonia oxidation were these isolated Cu ions in the *8r* cage of SSZ-13. We recently found that the occurrence of isolated dehydrated $[Cu^{2+}(OH^-)]^+$ species is also likely upon O_2-activation of Cu-SSZ-13 (Si/Al = 13.1, Cu/Al = 0.44); from UV-Vis analysis we also ruled out the presence of Cu−O−Cu dimeric species in SSZ-13. These species can instead readily form upon O_2-activation in Cu-ZSM-5 and Cu-

beta zeolites characterized by a similar Cu and Al content.[15] Very recently, Andersen *et al.*[16] demonstrated the presence of significant amount of Cu located at a specific crystallographic site in the *8r* (~80% of the Cu) by Rietveld/MEM analysis applied to synchrotron powder X-ray diffraction data of dehydrated Cu-SSZ-13 (Si/Al = 15.5, Cu/Al = 0.45, similar to the sample investigate in our previous studies[15, 17] and in the present work). Based on DFT analysis, the authors assigned this site to $[Cu^{2+}(OH^{-})]^{+}$ complexes, preferentially stabilized in proximity of an isolated Al T-site in the *8r* unit. The presence of a major fraction (~ 50%) of Cu-sites in activated Cu-SSZ-13, that exist as $[Cu^{2+}(OH^{-})]^{+}$ species, EPR-silent due to Pseudo Jahn-Teller effect (PJTE), has been also recently proposed by Mossin *et al.*[18] to explain the loss of EPR signal upon thermal dehydration at 250 °C.

In partial contrast with the findings reported above, Verma *et al.*[19] performed a combined experimental (UV-Vis, XAS, catalytic measurements) and computational kinetic study of dry NO oxidation on Cu-SSZ-13 catalysts (Si/Al = 4.5), suggesting at least two Cu ion configurations within SSZ-13: for Cu/Al < 0.2, the dominant configuration should consists in dehydrated isolated Cu^{2+} ions, located in the vicinity of 2 framework Al sites, *i.e.* Al pairs, in the *d6r* units of SSZ-13. For Cu/Al = 0.2 all framework Al pairs in *d6r* units are ion-exchanged by dehydrated isolated Cu^{2+} ions. For Cu/Al > 0.2, the authors suggest the occurrence of Cu_xO_y species (per mole Cu, $x \geq 2$, $y \geq 1$), likely balanced by Al pairs in the 8-membered rings of SSZ-13.

From the scenario outlined above, it is clear that Cu speciation in dehydrated SSZ-13 zeolite is greatly affected by the composition of the zeolite in term of both Cu/Al and Si/Al atomic ratios. Unfortunately, the Al distribution in zeolites is not uniform and, besides few isolated exceptions,[20] it has been only described by a statistical point of view. Even though DFT calculations have been successfully employed for a theoretical description of different Cu sites,[21, 22] a detailed experimental analysis on the nature, local environment and structural parameters of dehydrated Cu species is still missing. Once the investigation of the NH_3-SCR reaction mechanism is concerned, the identification of the active sites of the catalyst is even more controversial. Indeed, several reaction cycles have been proposed so far[4, 7, 23, 24], involving a variety of intermediate Cu-species.

Herein we report a comprehensive FTIR, X-ray absorption (XAS)/emission (XES) and DFT study, with the aim to clarify Cu speciation in a dehydrated Cu-SSZ-13 sample characterized by Si/Al = 12 and Cu/Al = 0.44, which is of foremost importance as a key substrate for reliably closing the SCR cycle and thus designing more efficient $deNO_x$ catalysts. FTIR spectroscopy is particularly suited to identify the presence of specific species, and to monitor *in situ* the dehydration process,[25, 26] being perfectly complemented by XAS spectroscopy. Indeed, XAS is an ideal tool to elucidate the average electronic properties and coordination geometry of the metal sites, which demonstrated to be greatly helpful in tackling the inherent complexity of the most efficient catalysts.[27-29] When assisted by computational analysis, *in situ* XAS is indispensable to identify the quantitatively-dominant Cu-species formed in the catalyst after activation.[3, 14, 19, 22, 30-32] XES has proven to be an effective tool for local structure determination as well, since the probed high-lying valence orbitals are sensitive to chemical bonding.[28, 33-35] Being an independent element-selective method, it complements XAS data, making the combined analysis of XES, EXAFS and XANES more reliable. Noteworthy, a combined *operando* XAS/XES approach supported by DFT analysis recently allowed Grunwaldt and co-workers to disclose the mechanism of the NH_3–SCR over a Fe-ZSM-5 zeolite catalyst.[36]

Driven by these motivations, here we extended our recent combined *in situ* FTIR/XAS/XES and DFT study,[17] primarily focused on the interaction of the catalysis with ammonia, by reporting a detailed investigation of activated Cu-SSZ-13, both in term of final states and time/temperature-resolved evolution during the activation ramps. In addition, in this improved study we were able to conjugate XAS (in both the XANES and EXAFS regions) and XES analysis accessing combined information on oxidation state, density of occupied and unoccupied electronic states, local coordination geometry/symmetry and coordination number of Cu sites in the different conditions probed. Such a high level of information enabled a reliable DFT-assisted quantitative refinement of the Cu-environments most relevant to describe the average properties of the activated Cu-SSZ-13.

Activation performed in an oxidant atmosphere (50% O_2/He, herein referred to as *O_2-activation*) is the most relevant to the real lean SCR conditions of the catalyst. However, by comparing the response of the catalysis to different activation atmospheres, such as pure He flow (hereinafter, *He-activation*), key information on the nature of the Cu-sites can be obtained. In this respect, our investigation also provided novel insights on the mechanism of how Cu ions undergo the so called "self-reduction" upon He-activation, a key step which is crucial for the understanding of the Cu^{2+}/Cu^{+} redox chemistry occurring under SCR conditions.

Results and discussion

Infrared characterization of activated Cu-SSZ-13: evidences for an (OH) "extra-ligand"

FTIR spectra collected at different temperatures upon Cu-SSZ-13 dehydration in 50% O_2/He flow are reported in Fig. 1 (see ESI Sec. 1.2† for experimental details). Referring to spectrum collected at 30 °C (blue curve), bands due to molecularly adsorbed water are observed at 1623 (δ), 3200 (ν_s) and 3670 cm^{-1} (ν_{as})[37, 38] These bands can be associated to both water molecules physisorbed on zeolite channels and water molecules coordinated to copper sites as aquo-complexes. Broad features related to H-bounded hydroxyls appear in the 3200 – 2100 cm^{-1} range, while the contribution of framework modes, *i.e.* overtones ν(T–O–T), gives rise to four low intense bands at 1998, 1858, 1680 and 1535 cm^{-1}. Noteworthy, ν(OH)

contribution of silanols prevalently located on external surfaces of the zeolite is observed at 3737 cm^{-1} , indicating that only a fraction of these species are perturbed by water molecules *via* H-bonds at 30 °C.

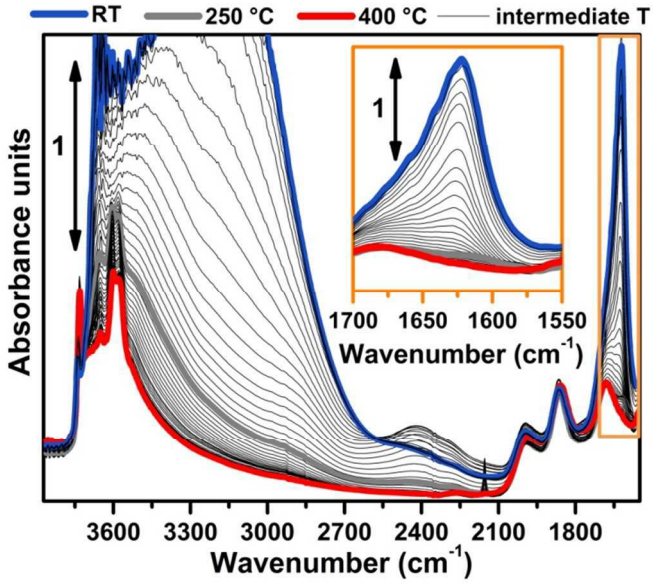

Fig. 1. Dehydration of Cu-SSZ-13 zeolite monitored by *in situ* FTIR spectroscopy. Sample was thermally treated by flowing 30 ml/min of 50% O_2/He. Spectra colour refers to different temperature: blue curve to 30°C, grey curve to 250°C, red curve to 400°C, black curves to intermediate temperatures. Inset reports a magnification of the signal related to δ(OH) mode of molecularly adsorbed water (spectral region highlighted by the orange box in the main panel).

Spectral changes upon zeolite dehydration could be described as follow: (i) gradual intensity decrease of the 3700, 3200, 3200 – 2100 cm^{-1} and 1623 cm^{-1} bands. The total disappearance of 1623 cm^{-1} at 250 °C (grey curve) is a strong indication that molecular water is almost completely desorbed at this temperature (see also the magnification in the inset of Fig. 1). (ii) Gradual appearance of 3611 and 3584 cm^{-1} bands related to ν(OH) of not H-bonded bridged hydroxyls groups with a strong Brønsted acidity.[15, 39]

In order to investigate the effects of different pre-treatments, Fig. 2 reports the FTIR spectra of dehydrated Cu-SSZ-13 zeolite collected upon O_2-activation and He-activation at 400 °C. For sake of comparison the spectrum of O_2-activated H-SSZ-13 zeolite is also reported. All the spectra show common bands related to ν(O–H) modes of silanols (3737 cm^{-1}) and Brønsted sites (3611 cm^{-1}, 3584 cm^{-1}).[15, 39] In addition, the spectrum of O_2-activated Cu-SSZ-13 shows two distinct features at 3656 and 905 cm^{-1} which are not observed in the other cases. As we recently pointed out, the 3656 cm^{-1} feature only appears upon oxidative thermal treatment of the zeolite and it can be considered as a fingerprint of $[CuOH]^+$ species stabilized in the SSZ-13 matrix.[15] On the base of previous studies,[40] the band at 905 cm^{-1} can be tentatively assigned to δ(O–H) mode of the same species. It is important to note that a similar set of bands have already been observed for other metal containing zeolites, and they have been assigned to corresponding M–OH species.[40-42] The fact that these bands do not appear when the sample undergoes "self-reduction" upon He activation (see black curve in Fig. 2), suggests that the stabilization of the OH extra-ligand on Cu(I) state is unlikely.

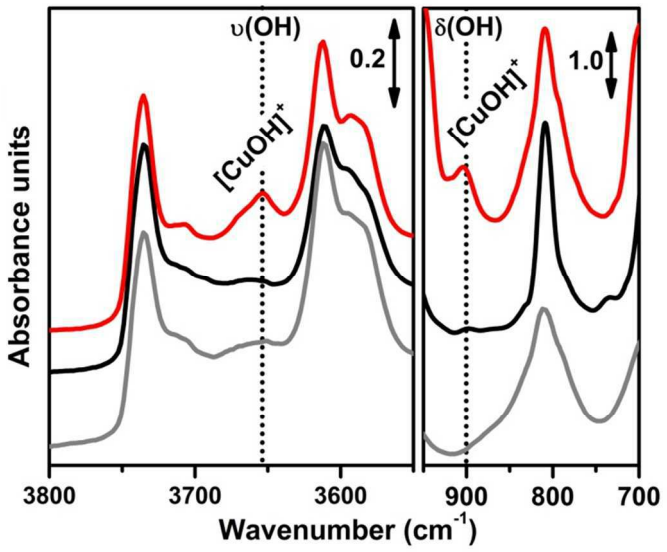

Fig. 2. FTIR spectral evidences of $[CuOH]^+$ species in O_2-activated Cu-SSZ-13 zeolite (red curve). Spectra are reported in both ν(OH) (left part) and δ(OH) (right side) regions. For sake of comparison the spectra of He-activated Cu-SSZ-13 (black curve) and H-SSZ-13 (grey curve) zeolites are also reported; the spectra have been vertically shifted for clarity. In Cu-SSZ-13 zeolite the bands related to $[CuOH]^+$ species only appear upon O_2-activation at 3655 and 905 cm^{-1}.

Looking at the 3611 and 3584 cm^{-1} bands related to Brønsted sites, it is important to note that the intensity of these bands in dehydrated Cu-SSZ-13 is surprisingly high and only slightly lower compared to the parent material H-SSZ-13 (Fig. 2, grey curve). This is interesting since the intensity of these bands is expected to decrease consistently in a sample characterized by a Cu/Al ratio of 0.444. Indeed, it is generally assumed that when copper is introduced in the zeolite framework upon aqueous ion exchange, the positive charge (+2) of hydrated Cu^{2+} ions must be balanced by two negative charges, likely represented by two Al atoms in close proximity. Therefore, a ratio of Cu^{2+}/Al^{3+} = 0.5 should represent the total ion exchange level. Conversely, our results clearly show that a consistent concentration of not exchanged sites, *i.e.* H^+ of Brønsted sites, is still present even if the Cu^{2+}/Al^{3+} ratio is not far from the stoichiometric exchange level. This evidence, together with the strong insights supporting the formation of $[CuOH]^+$ as dominant species upon O_2-activation, can be explained according to two possible mechanisms. In those sites characterized by 2 Al atoms in a close proximity (**2Z**$^-$), the stabilization of divalent $Cu^{2+}(H_2O)_n$ complexes upon ion exchange procedure is favored; the gradual dehydration of these complexes leads to water dissociation in $[CuOH]^+$ and H^+ species, eq. (1), where the latter is assumed to balance the charge of one of the two framework Al atoms. According to FTIR analysis (see Fig. 2), at 250 °C copper sites can be considered fully dehydrated; for T > 250 °C $[CuOH]^+$ species can only be stabilized in a oxidative atmosphere,

otherwise they undergo "self-reduction" as a consequence of OH extra-ligand loss. Alternatively, dehydration of $Cu^{2+}(H_2O)_n$ complexes could lead to bare Cu^{2+} cations, eq. (1a). Conversely, in those sites characterized by only 1 Al (**1Z**$^-$), the hydrated state upon aqueous ion exchange is likely represented by monovalent $[Cu^{2+}(H_2O)_n(OH)]^+$ complexes. In this case, the formation of $[CuOH]^+$ upon dehydration does not require any water dissociation, eq. (2), and the concentration of Brønsted sites in the dehydrated material is the one predicted from a total exchange level of $[CuOH]^+/Al^{3+} = 1$. In all these cases, the loss of the OH extra-ligand results in the reduction of the Cu^{2+} centre to Cu^+.

$$2\boldsymbol{Z}^-: Cu^{2+}(H_2O)_n \rightarrow Cu^{2+}(H_2O) + (n-1)(H_2O)^{\uparrow} \rightarrow [CuOH]^+ + H^+ \rightarrow Cu^+ + (OH)^{\uparrow} + H^+ \quad \text{eq. (1)}$$

$$2\boldsymbol{Z}^-: Cu^{2+}(H_2O)_n \rightarrow Cu^{2+} + n(H_2O)^{\uparrow} \quad \text{eq. (1a)}$$

$$1\boldsymbol{Z}^-: [Cu^{2+}(H_2O)_n(OH)]^+ \rightarrow [CuOH]^+ + n(H_2O)^{\uparrow} \rightarrow Cu^+ + (OH)^{\uparrow} \quad \text{eq. (2)}$$

The reversibility of the OH extra-ligand loss has been confirmed by XAS and FTIR, demonstrating that Cu^+ sites rapidly undergo re-oxidation with consequent restoring of $[CuOH]^+$ species if they are exposed to a gas mixture of O_2/H_2O (see ESI Fig. S5a,b†).

Comparison between O_2-activation and He-activation as monitored by XAS: final states and evolution

Fig. 3 reports a comparison between the XANES and EXAFS spectra collected for the initial (hydrated) and final states of the two activation process, namely under O_2-activation and He-activation conditions (see ESI Sec. 1.3† for experimental details). The characteristic XANES features occurring in the three probed states of the catalyst are the same as observed in our previous study,[17] where they have been assigned on the basis of the broad literature on Cu K-edge XANES in metal-exchanged zeolites[22, 43-49] and other systems.[50, 51]

As expected from previous investigations by us[17] and others[22, 30, 32], both XANES and EXAFS spectrum of the hydrated material (Fig. 3a and b, respectively, blue lines) closely resemble the spectra collected on a Cu(II)-acetate aqueous solution (see ESI Fig. S4†), where no significant differences can be identified within the available data quality. The structure of hydrated Cu(II) ions has been thoroughly analyzed in previous XAS studies[52-55] and, despite being an elementary case in chemistry, it represents an ongoing challenge for EXAFS and XANES analysis. In particular, the most recent reports suggest a dynamical equilibrium between Cu(II) sites 6-, 5- and even 4-coordinated to O atoms from H_2O molecules. A preferred configuration was hardly discriminated even with the most sophisticate XANES analysis approaches[54, 55]. The similarity in the XAS spectra demonstrates that equivalent conditions are locally verified also in hydrated Cu-SSZ-13, crowded with highly mobile Cu(II) aquo-complexes, resulting in a first-shell magnitude of the $|FT(k^2\chi(k)|$ spectrum compatible with time-averaged coordination to 5 O ligands. Here, no evidence of interaction with the zeolite framework is observed, due to the absence of well-defined coordination shells at higher R-distances.[17, 22, 30, 32] Unfortunately, it is impossible to distinguish by XAS the $[Cu(H_2O)_{n-1}(OH)]^+$ and $[Cu(H_2O)_n]^{2+}$ complexes (with n ranging from 4 to 6), due to the weak scattering amplitude of H.

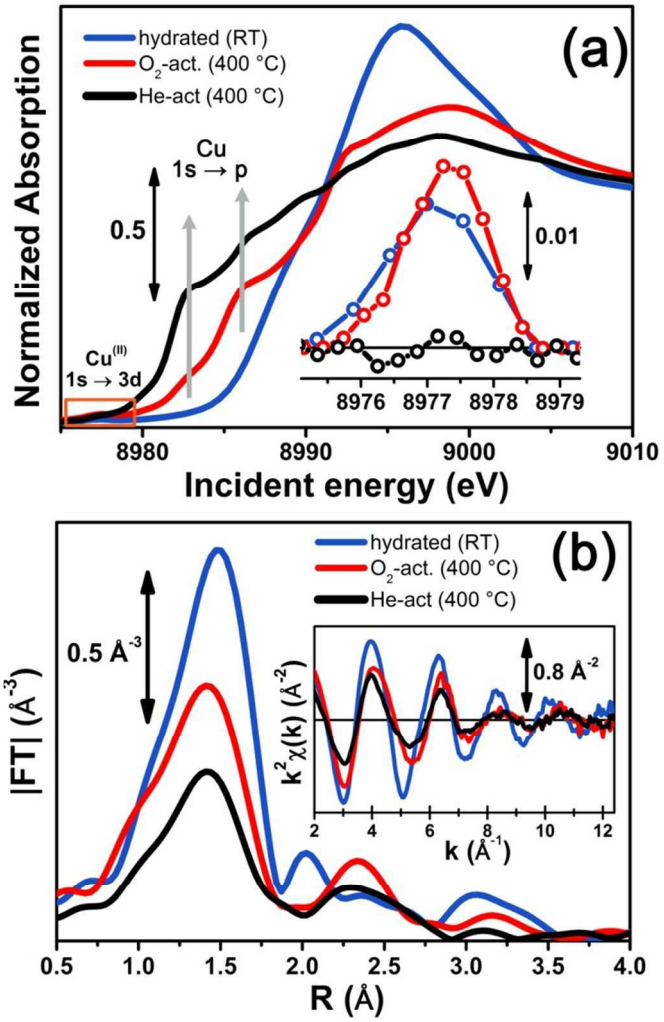

Fig. 3. *In situ* static XAS data collected on the hydrated (RT), O_2-activated and He-activated (400 °C) Cu-SSZ-13 catalyst. (a) Cu K-edge XANES spectra; the inset reports a magnification of the background-subtracted pre-edge peak highlighted by the orange box in the main panel. (b) Magnitude of the FT EXAFS spectra, obtained by transforming the k^2-weighted $\chi(k)$ curves reported in the inset in the (2.4 – 12.4) Å^{-1} range.

O_2-activation resulted in a XANES spectrum fully in line with that previously reported by us[17] and others,[14, 22] (Fig. 3a, red line) pointing out the effectiveness of an oxidant atmosphere in the inhibition of the "self reduction" effect[48, 56] during Cu-SSZ-13 activation. The XANES signature of the O_2-activated catalyst is typical of Cu(II) sites in a less coordinated environment, characterized by a lower symmetry[48, 51, 56, 57] with respect to that associated to the hydrated material.

Conversely, He-activation resulted in the typical XANES spectrum of Cu(I) sites in non-linear, low-coordination number configurations,[50, 58, 59] with a prominent and highly-structured pre-edge region developing from ~ 8982 eV, consistent with that observed upon *in vacuum* activation in our previous study.[17] Noteworthy, in the present experiment we achieved a more complete reduction of Cu-centres with respect to the *in vacuum* activation, by prolonged waiting in He flow at 400 °C. Indeed, no detectable peak in correspondence of the *1s* → *3d* transition, which fingerprints the presence of Cu(II),[43, 44, 50, 51] was observed in the background-subtracted XANES spectrum of He-activated Cu-SSZ-13 (see Fig. 3a, inset). Residual signal from this peak after activation in He was visible only in high energy resolution fluorescence detected (HERFD) XANES spectra, due to the significantly decreased background in the pre-edge region (see experimental spectrum in Fig. 10b). Presumably, it originates from small fractions (indicatively ≤ 10 % at. Cu for each species) of still-oxidized Cu species, such as isolated Cu(II) sites (most likely in the *d6r*, charge-balanced by 2 Al atoms), CuO nano-clusters or Cu–O–Cu dimers, as also recently evidenced by EPR [18] and XRD[16] studies on Cu-SSZ-13 samples with equivalent Si/Al and Cu/Al ratios. Being structurally flexible, inhomogeneous and minor, the latter multi-nuclear Cu-species may escape detection by EXAFS, despite the presence of high-amplitude metal-metal scattering paths.

Very interestingly, EXAFS shows a substantial lowering of the first shell magnitude after both activations with respect to the hydrated state (see Fig. 3b), which is clearly more pronounced for the He-activated sample. This novel evidence is crucial to correlate the Cu(II) → Cu(I) reduction to the "extra-ligand" loss mechanism suggested by FTIR results, which is promoted or inhibited depending on the atmosphere, either oxidant or inert, in which the thermal treatment is conducted. Moreover, EXAFS evidences the interaction of Cu-centres with the framework after both activations, with the appearance of a well-defined second coordination shell in the 2 – 3 Å region of the phase uncorrected $|FT(k^2\chi(k)|$ spectra. EXAFS fits reported in the following confirmed this assignment, indicating a major contribution from the single scattering (SS) paths involving the nearest neighbour T (T = Al, Si) atom(s) around Cu sites in the *d6r* and *8r* units of the SSZ-13 zeolite.

More detailed insights can be obtained by monitoring *in situ* the evolution of the XANES and EXAFS spectra collected during the O_2-activation and He-activation ramps, summarized in Fig. 4. We will first focus on the O_2-activation process, and then discuss the additional modifications observed during activation in He flow.

The evolution of the XANES features (Fig. 4a) is consistent with a progressive dehydration process, where the water molecules in the Cu(II) hydration sphere are progressively removed, as evidenced by the decrease of the intense white line characteristic of the hydrated material. Simultaneously, the partially dehydrated Cu(II) ions are adopting specific positions in the framework, in a less symmetric coordination environment with respect to the hydrated condition. The lowering in coordination symmetry upon dehydration is reflected by the developing of a pre-edge shoulder assigned to *1s* → *p* transitions in the 8985 – 8990 eV range, typical of Cu(II) sites.[60] In addition, the Cu(II) fingerprint peak at ca. 8977.5 eV slightly grows in intensity with increasing temperature, which is also consistent with a less symmetric Cu coordination geometry. The evolution of the XANES features during O_2-activation is qualitatively in agreement with what has been recently reported by Kwak *et al.*[32] for Cu-SSZ-13 (Si/Al = 6, Cu/Al = 0.4). Combining XANES, TPD-XRD and *in situ* DRIFT measurements, the authors confirmed that upon dehydration Cu^{2+} ions migrates into cationic positions where they strongly interact with the zeolite framework, although they did not quantitatively tested specific structural environments for the activated Cu-centres. Aiming to more detailed structural insights, we will use EXAFS to determine the dominant coordination environment of the metal, and how it evolves during activation, as a practical way for structural refinement.

In particular, the FT EXAFS spectra collected on our Cu-SSZ-13 sample during O_2-activation (Fig. 4b) shows a progressive decrease of the first coordination shell, resulting from Cu–O single scattering (SS) paths (qualitatively from an oxygen coordination number N_O ~ 5 to N_O ~ 3, see below for quantitative fitting). The reduction in the first shell amplitude is accompanied by the modifications of the signal in the (2 – 3) Å region, where the unstructured signal characteristic of the hydrated material (mainly resulting from multiple scattering (MS) paths associated with linear O–Cu–O configurations involving the $O(H_2O)$ ligands in the equatorial plane of the aquo-complex[53]) is progressively replaced by the well-defined coordination shell associated with increased interaction with the framework.

It is important to note that, for the O_2-activated material (Fig. 4a,b), both for XANES and EXAFS, the major evolution is observed in the RT – 250 °C temperature range, whereas the spectral feature are only slightly modified increasing the temperature up to 400 °C. Here, the small intensity loss of the EXAFS FT signal is due only to the increase of the Debye-Waller (DW) factors with temperature. Interestingly, FTIR data reported in Fig. 1 clearly show that at 250 °C no more adsorbed molecular water is present in the system: the dehydration of Cu(II) centres is thus completed, and the metal ions are likely already set in well-defined positions in the zeolite units.

Differently to what observed in an oxidant atmosphere, the evolution of the XANES and EXAFS features during He-activation can be rationalized only considering two distinct steps. The first step, which we will refer to as *dehydration,* occurs from RT to ~ 250 °C, while from 250 °C up to 400 °C we identified a *reduction* step.

The *dehydration* step is fully equivalent to what observed during O_2-activation. The XANES and EXAFS spectra collected at the final state of the O_2-activation are reported for comparison as red dashed lines in Fig. 4c, d, respectively: it can be clearly observed that the final state obtained upon stabilization in O_2/He flow at 400 °C is equivalent to the intermediate state reached at ~ 270° C in He flow.

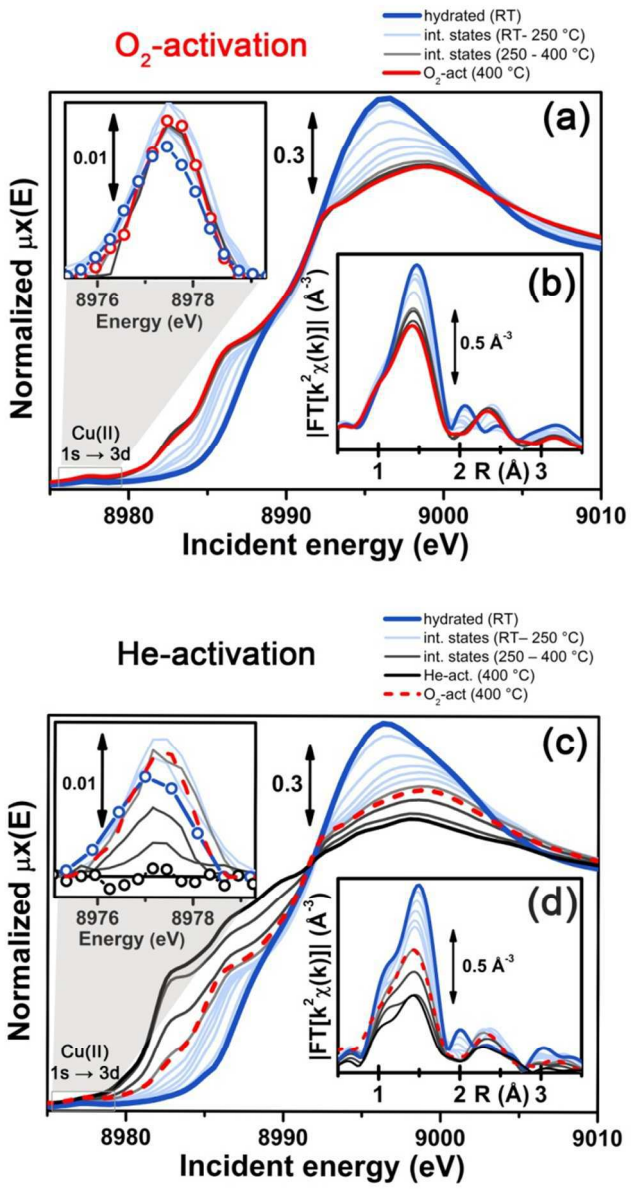

Fig. 4. *In situ* temperature-dependent XAS data collected during O_2-activation and He-activation processes. (a, b) XANES spectra, part (a), and magnitude of the FT of the k^2-weighted $\chi(k)$ EXAFS curves, performed in the (2.4 – 12.4) $Å^{-1}$ range, part (b), measured during O_2-activation of the Cu-SSZ-13 catalyst. The inset of part (a) reports a magnification of the background-subtracted Cu(II) 1s → 3d pre-edge peaks highlighted by the grey box in the main panel, for selected intermediate temperature steps. (c, d) As parts (a, b) but for He-activation of the Cu-SSZ-13 catalyst. The final spectrum collected on the O_2-activated Cu-SSZ-13 sample at 400 °C is also reported for comparison in panels (c, d).

The evolution of the system during activation in the 250 – 400 °C range is then dramatically different depending on the atmosphere in which the process is conducted. In particular, in the case of O_2-activation we observed a stabilization of the spectral features, while for activation in He flow, the XANES features showed pronounced modifications as a function of the temperature (Fig. 4c), including the development of pre-edge peaks in the 8982 – 8990 eV range, with intensities and energy positions associated to Cu(I) species. Simultaneously, a steep decrease in the intensity of the Cu(II) fingerprint peak at ~ 8977.5 eV is observed, which unambiguously demonstrates the Cu(II) → Cu(I) *reduction*, involving progressively more and more Cu-sites as the temperature increases, up to a virtually-complete erosion.

Importantly, during the *reduction* step EXAFS spectra showed a further decrease in the first-shell magnitude with respect to the final state reached after O_2-activation (Fig. 4d), consistent with the loss of one out of ~ 3 O ligands in the first coordination shell of the Cu sites being reduced once completely dehydrated.

Summarizing, the above presented combined XANES and EXAFS evidences are in full agreement with FTIR results, and strongly support the formation of Z−$[CuOH]^+$ complexes at the end of the *dehydration* step up to ca. 250 °C, according to the routes proposed in eq. (1) and eq. (2). The stabilization of these species in the proximity of $\mathbf{1Z^-}$ sites, balancing the charge of the $[CuOH]^+$ complex, is highly favored during oxidative thermal treatment. Conversely, when the dehydrated catalyst is further heated in an inert atmosphere, Cu(II) centres gradually undergo reduction, which likely occurs *via* homolytic cleavage of the Cu−OH bond[18, 46] and loss of the (OH) "extra-ligand", leaving "bare" Cu(I) sites in their pristine framework location. Noteworthy, these sites showed a strong propensity toward re-oxidation once the gas flow is switched from pure He to a O_2/He + 5 % H_2O mixture. As shown in ESI Fig. S5a†, in these conditions at 400 °C the XAS signature of the final Cu(II) state observed at the end of O_2-activation was quickly restored. Following the same experiment by FTIR spectroscopy, the reappearance of the $[CuOH]^+$ fingerprint band at 3656 cm^{-1} is readily observed (see ESI Fig. S5b†).[15] These results reinforce the evidence for a direct connection between the oxidation state of the Cu-centres and the coordination of an extra-ligand group. Contextually, it is important to emphasize that the extra-ligand loss with consequent reduction of $[CuOH]^+$ species can also occur in the dehydrated material: Fig. S5c in ESI† clearly shows that Cu(I) XAS features were gradually restored if the O_2-activated material, *i.e.* containing an high fraction of $[CuOH]^+$ species, is contacted with an He flow at 400 °C. This result is in contrast with the belief that Cu sites could be self-reduced by carbonaceous deposits left in the zeolite along the preparation and/or by hydrocarbon impurities adsorbed from the atmosphere.[61] Indeed, this kind of species is not expected to persist upon O_2-activation procedure at 400°C.

Having in mind these considerations, in the followings we will investigate in more details the coordination environments of Cu(II) and Cu(I) ions in Cu-SSZ-13 by DFT, on the basis of the principal configurations proposed in the literature. Hence, the resulting candidate structures will be systematically tested by EXAFS fits and XANES/XES simulations, aiming to achieve the best reproduction of the X-ray spectra collected on the catalysis after O_2-activation and He-activation.

DFT-based modeling of the possible Cu(II) and Cu(I) sites in activated Cu-SSZ-13

In our computational screening (see ESI Sec. 1.4.1† for details), we considered the two principal locations for the Cu ions in the CHA framework which were proposed in previous theoretical[21, 22] and experimental studies,[3, 4, 13, 31] *i.e.* the planes of the *d6r* and *8r*. Hence, we envisaged two possible configurations for balancing the charge of Cu^{2+} and Cu^{+} centres, resulting from O_2-activation and He-activation as clearly shown by XANES. In particular, we considered: (i) only the charge-compensating effect of Al atoms located in the same unit in which Cu is hosted or (ii) the combination of the effect of the Al atoms in the proximity of Cu sites and the presence of an $(OH)^-$ extra-ligand coordinated to the Cu centre. The resulting DFT-optimized geometries, accounting for all the possible configurations according to Lowenstein's rule,[62] are reported in Fig. 5.

Under the previous assumptions, Cu(II) sites could be obtained by stabilizing a $[CuOH]^+$ complex in proximity of a (**1Z**$^-$) site (*d6r1AlOH* and *8r1AlOH* models in Fig. 5) or hosting a "bare" Cu^{2+} cation next to a (**2Z**$^-$) site (*d6r2Al#1,2* and *8r2Al#1-3* models in Fig. 5). Conversely, for Cu(I) sites only the configuration with a "bare" Cu^+ cation next to a (**1Z**$^-$) site is available, both in the *d6r* and *8r* units (*d6r1Al* and *8r1Al* models in Fig. 5). For additional explanation on the nomenclature adopted for the different DFT-models, see ESI Sec. 4, Scheme S1†. The average bond distances for the principal shells of atomic neighbours surrounding the Cu centres observed for all the DFT-optimized geometries are reported in Table 1, whereas a complete report on the individual bond lengths and a detailed description of the different configurations can be found in ESI Sec. 4†.

Once DFT has been employed to obtain a set of stable configurations, EXAFS fitting of the spectra collected after O_2-activation and He-activation provided an effective and computationally-inexpensive way to perform a wideband screening of the possible candidates models (see ESI Sec. 1.4.2† for details on the fitting procedure). Subsequently the simulations of XANES and XES were performed for the same structures. The motivation for that was the higher sensitivity of these methods to coordination bond angles with respect to EXAFS. Thus, the goal was to discriminate between the DFT structures with similar coordination numbers, but substantially different three-dimensional arrangement of the ligands. It is worth to note that for each structure the whole optimized cluster was taken into account in order to perform XANES and XES calculations (ESI Sec. 1.4.3†), in contrast to EXAFS where only the atoms of the corresponding ring at distances up to 3.5 Å from Cu were considered.

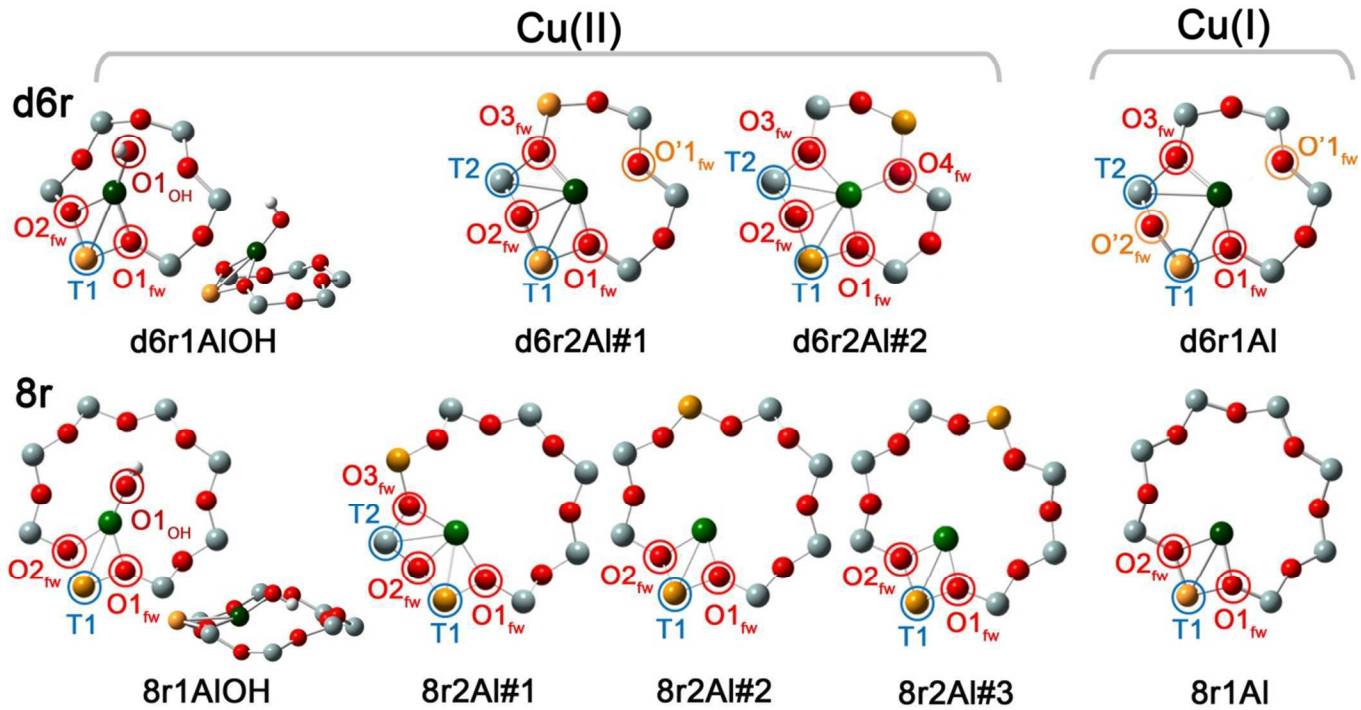

Fig. 5. DFT-optimized structures highlighting the local coordination environment of Cu(II) and Cu(I) sites in the *d6r* and *8r* units of the CHA framework. Atom colour code: Cu, green; H, white; O, red; Al, gold, Si, gray. Coloured circles highlight the principal shells of atomic neighbours surrounding the Cu centres, for which average bond distances are reported in Table 1.

Table 1. DFT-optimized average bond distances from Cu and coordination numbers for the principal shells of atomic neighbours surrounding Cu(II) and Cu(I) centres in the *d6r* and *8r* units of the CHA framework. See Fig. 5 for the atoms labeling code.

	Cu(II) sites models							Cu(I) sites models	
Model parameters	*d6r1Al OH*	*d6r2Al #1*	*d6r2Al #2*	*8r1Al OH*	*8r2Al #1*	*8r2Al #2*	*8r2Al #3*	*d6r1Al*	*8r1Al*
N_{OH}	1			1					
Cu–O_{OH} (Å)	1.774	–	–	1.757	–	–	–	–	–
$N_{O(fw)}$	2	3	4	2	3	2	2	2	2
<Cu–O_{fw}> (Å)	1.982	1.974	2.028	1.990	2.030	1.933	1.938	1.957	1.962
$N_{O'(fw)}$	–	1						2	
<Cu–O'_{fw}> (Å)	–	2.393	–	–	–	–	–	2.511	–
N_T	1	2	2	1	2	1	1	1	1
<Cu–T> (Å)	2.782	2.714	2.805	2.690	2.655	2.681	2.707	2.811	2.709

EXAFS fitting for O_2-activated and He-activated Cu-SSZ-13

O_2-ACTIVATED CU-SSZ-13: EXAFS SCREENING OF DIFFERENT DFT-OPTIMIZED MODELS FOR CU(II) SITES.

Fig. 6 summarizes the results obtained by fitting the experimental EXAFS spectrum collected at 400 °C on O_2-activated Cu-SSZ-13 on the basis of the previously reported DFT-optimized models for Cu(II) sites in the *d6r* and 8r units. A full report on the optimized parameters resulting from the seven fits performed can be found in ESI Sec. 5†. From the graphical summary reported in Fig. 6, we realize that the configurations corresponding to a first-shell coordination number $N_{O(fw)}$ = 4 and $N_{O(fw)}$ = 2 (mostly associated to distant (**2Z**$^-$) sites in the larger *8r* units) resulted in S_0^2 values of ~ 0.8 and ~ 1.6, respectively. Conversely, when three-coordinated Cu(II) sites are considered (bonded to three O_{fw} atoms or to two O_{fw} atoms and to the $(OH)^-$ extra-ligand at a slightly shorter distance), S_0^2 values equal to the optimal value of ~ 1 within their errors are observed. Hence, the fit results support the stabilization of 3-coordinated Cu(II) sites after O_2-activation, thus ruling out the configurations involving 2- and 4-coordinated Cu-centres, at least as dominant structural components in our experimental conditions. This is in agreement with previous EXAFS studies on O_2-activated Cu-SSZ-13, which reported an average first-shell oxygen coordination number around three[3, 14]. However, this result was preferentially associated to bare isolated Cu(II) sites in the *d6r* (equivalent to our *d6r2Al#1,#2* models) whereas, to the best of our knowledge, the OH-like models, which exhibit a very similar first shell coordination, have never been considered as plausible alternatives for the interpretation of the EXAFS signal of the O_2-activated catalyst.

Among the favored 3-coordinated configurations, the *8r2Al#1* model provided an unsatisfactory fit due to a drastic increase of the R-factor value (R = 0.0180) with respect to the other geometries tested, and also due to a severe damping of the two SS Cu–T contributions by unreliably high DW values. Conversely, the lowest R-factor overall was found for the *8r1AlOH* model (R = 0.0022), evidencing an excellent line-to-line agreement between experimental and best-fit spectrum (see Fig. 7b,c). An almost equivalent R-factor was observed considering both the formation of the $[CuOH]^+$ complex in the *d6r* (model *d6r1AlOH*, R = 0.0035) and the stabilization of the cation next to (**2Z**$^-$) sites in the *d6r,* in the Al–T–Al configuration (model *d6r2Al#1*, R = 0.0030).

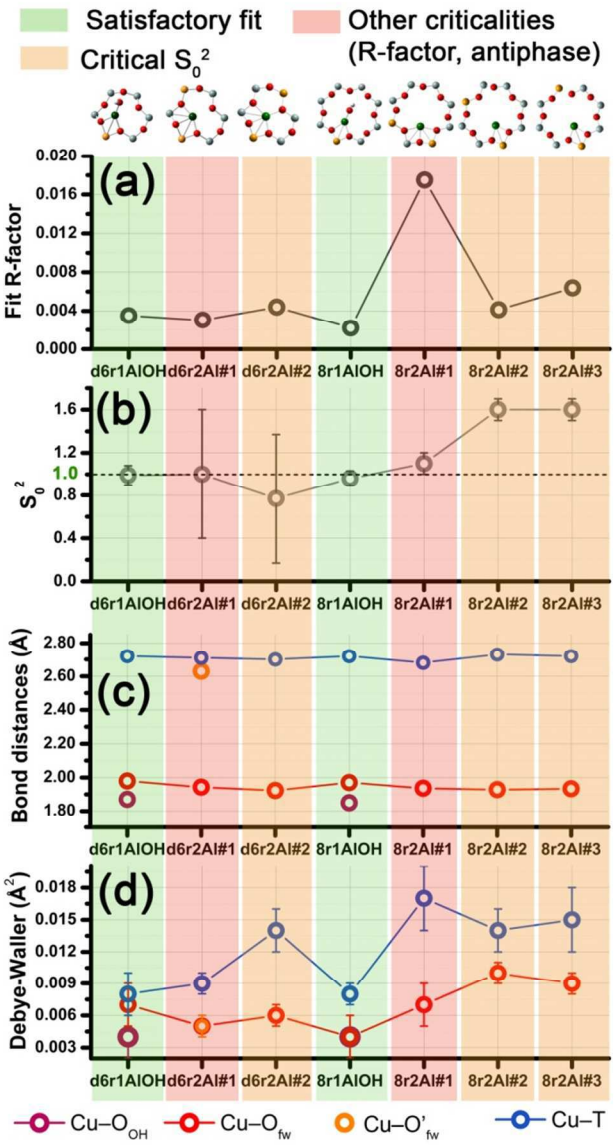

Fig. 6. Graphical summary of the results obtained by fitting the experimental EXAFS spectrum collected at 400 °C on O_2-activated Cu-SSZ-13 on the basis of the different DFT-optimized models for Cu(II) sites in the *d6r* and *8r* units of the CHA framework. In correspondence of each model we report: (a) the fit R-factor values; (b) the passive amplitude reduction factor S_0^2 (ideally equal to one, S_0^2 >1

suggest underestimated coordination numbers in the model, whereas $S_0^2 < 1$ indicates overestimated coordination numbers); (c) the average EXAFS-optimized bond distances and (d) DW factors for each coordination shell included in the fitting model. Vertical stripes of different colours are used to highlight the reliability level of the different fits, with the following colour code: satisfactory fits, green; fits resulting in critical S_0^2 values: orange; fits showing other criticalities, *e.g.* remarkable increase in R-factor value or strong antiphase effects, red.

The two fits performed on the basis of the extra-ligand-like configurations resulted in very similar values for all the parameters optimized, reflecting the high similarity of the two local environments around Cu(II) sites in both *d6r* and *8r*. Here, only slight deviations from the structural minima found by DFT ($\Delta R_i < 0.1$ Å) and reliable DW factor values (consistently with high-temperature data collection) were observed. As an example, Table 2 reports the best-fit parameters obtained for the *8r1AlOH* case. In addition, in Fig. 7b,c we compare the experimental magnitude and imaginary parts of the FT spectrum of the O_2-activated Cu-SSZ-13 catalyst to the corresponding best fit curves obtained for the *8r1AlOH* model. The individual SS paths contributions to the total signal from each included shell of neighbouring atoms are also shown.

Table 2. Best-fit parameters optimized by EXAFS fits of the k^2-weighted spectrum of O_2-activated Cu-SSZ-13 (data collection at 400 °C), employing as starting guess two selected DFT-optimized geometries for Cu(II) sites, *i.e.* the *8r1AlOH* and *d6r2Al#1* models (a detailed report on the EXAFS fits performed from all the Cu(II) models tested is reported in ESI Sec. 5†). The fit was performed in R-space, in the range (1.0 – 3.2) Å, employing the *k*-range (2.4 – 12.4) $Å^{-1}$ for the FT, resulting in a maximum number of independent parameters equal to $N_{ind} = 2\Delta k\Delta R/\pi = 14$.

Best fit parameters for O_2-activated Cu-SSZ-13 - Cu(II) sites		
Optimized parameters	*8r1AlOH*	*d6r2Al#1*
S_0^2	0.96 ± 0.07	1.00 ± 0.06
ΔE (eV)	– 1.8 ± 0.6	– 1.4 ± 0.9
R-factor	0.00220	0.00304
N_{par}	10	9
R_{OH} (Å)	1.85 ± 0.02	–
σ^2_{OH} ($Å^2$)	0.004 ± 0.002	–
N_{OH}	1	–
$<R_{O(fw)}>$ (Å)	1.97 ± 0.01	1.94 ± 0.01
$\sigma^2_{O(fw)}$ ($Å^2$)	0.004 ± 0.002	0.005± 0.001
$N_{O(fw)}$	2	3
$R_{O'(fw)}$ (Å)	–	2.63 ± 0.01
$\sigma^2_{O'(fw)}$ ($Å^2$)	–	0.005± 0.001
$N_{O'(fw)}$	–	1
$<R_T>$ (Å)	2.72 ± 0.01	2.71 ± 0.02
σ^2_T ($Å^2$)	0.008 ± 0.001	0.009± 0.001
N_T	1	2
α_{fw}	– 0.01 ± 0.01	– 0.03 ± 0.11
σ^2_{fw} ($Å^2$)	0.022 ± 0.005	0.05 ± 0.5
N_{fw}	4	6

For the *8r1AlOH* model the EXAFS-refined parameters are in good agreement with the DFT-optimized bond distances. In particular, the highest deviation is observed in correspondence of the Cu–O_{OH} bond, refined to (1.85 ± 0.02) Å, with respect to the (1.76 ± 0.02) Å value from DFT analysis. The bond distances between the cation and the framework atoms are only minorly adjusted, with a slight contraction of the O_{fw} shell and a slight elongation of the Cu–Al distance.

The first maximum in the $|FT\{k^2\chi(k)\}|$ spectrum mostly results from the combination of partially overlapping SS paths involving the O_{OH} atom of the extra-ligand group and two O_{fw} atoms. As expected, the structural parameters of the O_{OH} and O_{fw} atoms are affected by rather high mutual correlations. However, test fits performed with three degenerate O_{fw} SS paths, considering an intermediate Cu–O distance of 1.98 Å as starting guess, resulted in a ~ 50 % increased R-factor value and a ~ doubled $\sigma^2_{O(fw)}$ value of (0.010 ± 0.001) $Å^2$. Hence, EXAFS is able to distinguish an oxygen ligand located at significantly shorter distance to Cu with respect to the two O_{fw} atoms.

Noteworthy, we could consider a (O^-) group as an alternative extra-ligand, charge balancing the Cu^{2+} cations in the proximity of (**1Z**$^-$) sites. Unfortunately, discrimination by XAS between the $(OH)^-$ and (O^-) extra-ligands in the Cu coordination sphere is unfeasible, due to the weak scattering amplitude of H. Nonetheless, by combining XAS and FTIR results we can safely state that for a major fraction of the sites the O_2-activation results in the formation of $[CuOH]^+$ species. Indeed, the presence of $(OH)^-$ groups on Cu in the O_2-activated Cu-SSZ-13 is unequivocally demonstrated by the appearance of the bands at 3655 and 905 cm^{-1}, assigned to the ν(O–H) and δ(O–H) modes in the $[CuOH]^+$ complex, respectively. Conversely, the stabilization of $[CuO]^+$ monomeric moieties would be incompatible with such vibrational fingerprints.

The second maximum in the experimental $|FT\{k^2\chi(k)\}|$ mainly derives from an individual Cu–Al SS path, with minor contribution on the low-R side from the tails of the first-shell Cu–O_{fw} paths, and on the high-R side from the SS involving the other O/Si atoms of the *8r* unit falling in the considered R-range (up to 3.5 Å from the Cu absorber). This assignment quantitatively confirms that the appearance of a well defined coordination shell in the (2.0–2.8) Å range (phase-uncorrected) during activation can be considered as a fingerprint for the increased interaction of the Cu ions with the zeolite framework[22], concomitantly to the progressive replacement of the $O(H_2O)$ ligands with the O_{fw} ones upon thermal dehydration.

It is worth to note that the high-scattering amplitude Cu–Cu SS paths of Cu–O–Cu dimeric species are also expected to fall in this R-space region, in correspondence of a quite broad distribution of Cu–Cu distances in the (2.73 – 2.91) Å range, according to the previous literature on Cu-zeolites.[44, 63-65] Nevertheless, the high quality of the EXAFS fits performed without considering any metal–metal scattering path allows to exclude a major contribution from such species in the O_2-activated Cu-SSZ-13 catalyst. A different behavior was observed *e.g.* in Cu-ZSM-5 and Cu-IM-5 zeolites with comparable Cu/Al ratio,[49] where the second coordination shell of the experimental $FT\{k^3\chi(k)\}$ EXAFS spectra was successfully fitted only including in the refinement both a Cu–Al and a Cu–Cu contribution. It is worth to note that the detection of a minor fraction of Cu(II) sites (indicatively < 10%

of the total) occurring as Cu_xO_y ($x = 2$, $y \geq 1$) species is beyond the sensitivity limit of the EXAFS technique, especially if flexible dimers with highly dispersed Cu–Cu bond distances are concerned. However, the occurrence of such species as a dominant structural component (indicatively > 50% of the total Cu sites probed by XAS) in activated Cu-SSZ-13 is incompatible with our XAS results, even under the assumption of a high dispersion. Indeed, if a high concentration of these species had been present, their structural flexibility would have resulted in dampened and broadened but still detectable Cu–Cu SS contributions.

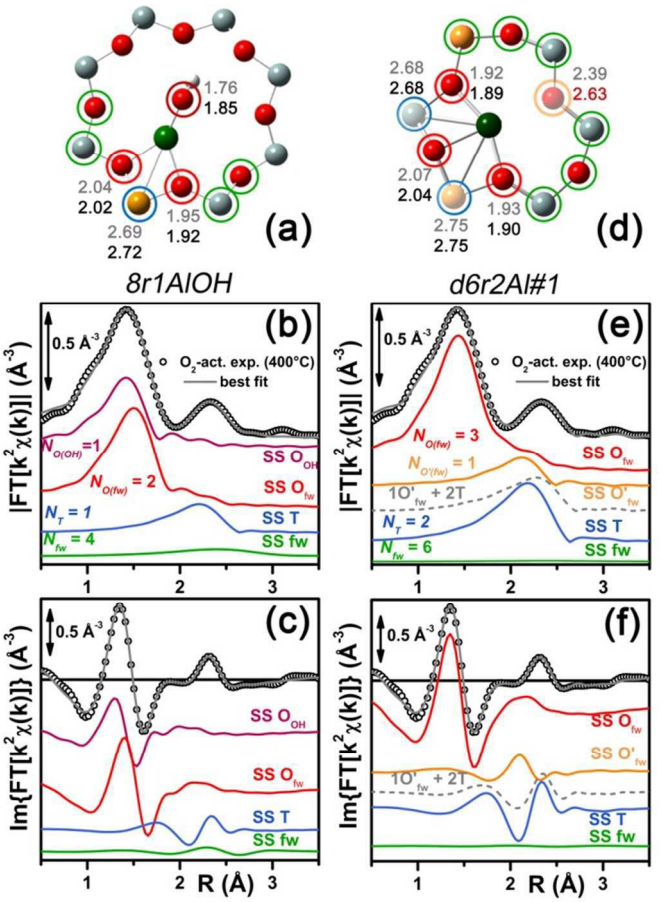

Fig. 7 (a),(d) Representation of the DFT-optimized (a) *8r1AlOH* and (d) *d6r2Al#1* geometries: atom colour code: Cu, green; H, white; O, red; Al, gold, Si, gray. Coloured circles highlight the different shells neighbouring atoms included in the fitting model. Starting DFT-optimized bond distances from the Cu absorber for each atom are reported in grey, while the correspondent values refined by EXAFS fitting are shown in black (distances are indicated in Å). (b),(c) Comparison between experimental EXAFS spectrum of the O_2-activated Cu-SSZ-13 catalyst and corresponding best fit performed from the *8r1AlOH* model; both modulus and imaginary parts of the FT are shown in part (b) and (c) respectively, together with the different SS paths contributions to the total signal, with the same colour code employed in part (a) and vertically translated for the sake of clarity. (f),(g) The same as parts (b),(c) but using the *d6r2Al#1* model as an input for the fit. Gray dashed lines indicate the residual signal after summing the O'fw and T contributions. For quantitative values of the parameters optimized in the two fits, see Table 2.

On this basis, the Cu–O–Cu dimers nestled in the *8r* cages, recently claimed by Verma *et al.*[19] to be the active sites for dry NO oxidation on Cu-SSZ-13 above Cu/Al atomic ratio = 0.2, could occur only as a minor fraction of the total Cu-sites in our Cu-SSZ-13 sample (Cu/Al = 0.44). In addition, preliminary XAS measurements on an O_2-activated low Cu-loading Cu-SSZ-13 sample (Cu/Al ~ 0.13) clearly show EXAFS features substantially equivalent to that reported here for the high-loading material (see ESI Sec. 6†). In particular, the EXAFS spectrum for the O_2-activated sample with Cu/Al ~ 0.13 always shows a well-defined coordination shell in the (2.0–2.8) Å range (phase-uncorrected), with comparable magnitude and only slightly shifted to higher distances. This evidence further discourages the possibility of a significant contribution by Cu–Cu SS paths from Cu–O–Cu dimers to such EXAFS feature in Cu-SSZ-13 catalysts even with a high Cu loading.

In summary, the *8r1AlOH* model provided a very good reproduction of the experimental spectrum collected on O_2-activated Cu-SSZ-13, with reliable value of all the physical and structural parameters refined and only minor deviations from the DFT-optimized geometry employed as starting guess in the fit. Equivalently good fits were obtained for the *d6r1AlOH* model (see ESI Sec. 5, Table S2†). Thus, in these conditions the *8r1AlOH* and *dr1AlOH* models can be hardly distinguished by EXAFS. However, it is worth to note that the Cu–T distance is refined to the same value of 2.72 Å starting from both DFT geometries, which foreseen Cu–T distances of 2.69 and 2.78 Å in *8r* and *d6r*, respectively. This suggests that the $[Cu^{2+}(OH)^-]^+$ complexes are preferentially stabilized in proximity of (**1Z**$^-$) sites in the plane of the larger *8r* units of the SSZ-13 framework, as also very recently confirmed by Andersen *et al.*[16] by Rietveld/MEM analysis of synchrotron powder X-ray diffraction data.

Apart from the two OH-like configurations, a very good line-to-line agreement between experimental and best fit lines was also obtained for the *d6r2Al#1* model, apparently without the occurrence of critical/unphysical values for the refined parameters (see Table 2 and Fig. 6). Consistently, such coordination environment for isolated Cu(II) sites in the *d6r* has been proposed as the dominant one in previous EXAFS works[3, 14], also based on its superior stability from DFT analysis. The experimental FT spectra of the O_2-activated Cu-SSZ-13 and corresponding best fit curves obtained for the *d6r2Al#1* model are also reported in Fig. 7,e,f together with the individual SS paths contributions from each shell of neighbouring atoms. Here, the first shell is successfully fitted by the SS contribution of three O_{fw} atoms refined at the average distance of (1.94 ± 0.01) Å by a slight contraction from the DFT values ($\Delta R_{O(fw)}$ = – 0.03 Å), with a DW factor $\sigma^2_{O(fw)}$ = (0.005± 0.001) Å^2, slightly increased with respect to the *8r1AlOH* case. However, the second coordination shell is reproduced only by a dramatic elongation of the Cu–O'$_{fw}$ distance up to (2.63 ± 0.01) Å ($\Delta R_{O'(fw)}$ = + 0.24 Å) with respect to the stable DFT configuration. Such a high distortion results in the almost perfect antiphase between the SS path involving the elongated O'$_{fw}$ and that involving the two T atoms, which on the contrary are left exactly in their original DFT positions. The effective signal which results from the partial cancellation of the two contributions is shown in Fig. 7e,f as a gray dashed line, and it is essentially equivalent to the SS path involving the individual Al atom in the *8r1AlOH* configuration (see parts b,c in the same figure). Noteworthy, suspiciously high correlations are also observed between the structural parameters of the O'$_{fw}$ and T shells ($\Delta R_{O'(fw)}$ & $\Delta R_T \rightarrow 0.95$). The destructive interference between EXAFS paths cannot be considered *a priori* as critical, and a few cases have been reported in which these severe "cancellation" effects are a distinguishing feature of the EXAFS signature for the studied material.[66-68] However this is

likely not the case, due to the drastic distortion of the *d6r* unit with respect to the DFT-optimized geometry and the similarity of the resulting signal in the (2.0–2.8) Å range to that resulting by an individual Al atom located at 2.72 Å from Cu, as in the *8r1AlOH and d6r1AlOH* models. In addition, test fits performed by modeling the Cu–O'$_{fw}$ SS path with an independent DW factor resulted in unphysically high values for the latter parameter. Even more drastically, by simply removing from the fit model this SS path, the fit was satisfactory, but with remarkably increased DW factor for the T shell (up to 0.016 Å^2) with respect to the extra-ligand-like configurations, probably to adjust the presence of two T atoms instead of one in the coordination shell of interest.

Based on these observations, our analysis strongly discourages the stabilization of a major fraction of Cu(II) sites next to (**2Z**$^-$) sites in the *d6r* according to the *d6r2Al#1* model after O_2-activation. If present, this configuration should involve a limited percentage of Cu sites, so that their contribution in the EXAFS spectrum could not be resolved within our data quality (a percentage of about 10% was recently suggested from EPR[18] and XRD[16] analyses performed on similar Cu-SSZ-13 samples, but using slightly different dehydration time/temperature conditions). Conversely, the formation of $[Cu^{2+}(OH)^-]^+$ complexes in *8r* units next to (**1Z**$^-$) sites ensures the best compatibility with our experimental spectrum and should be assumed as the most representative model for the average structural environment of Cu(II) sites in O_2-activated Cu-SSZ-13.

EXAFS ANALYSIS OF CU(I) SITES IN THE *D6R* AND *8R* UNITS

We tested the compatibility of the DFT-optimized models for "bare" Cu(I) sites in the proximity of (**1Z**$^-$) site in both *d6r* and *8r* by fitting the EXAFS spectrum collected on the He-activated catalyst. These configurations could be reached upon the progressive release of the extra-ligand group and subsequent readjustments of the reduced cation in its framework positions, as supported by the evolution of the XAS features during He-activation (see Fig. 4). Table 3 reports the respective best-fit parameters obtained on the basis of the *8r1Al* and *d6r1Al* models, while the corresponding best fit curves are reported in Fig. 8. Both the models were found to be compatible with the experimental spectrum, with S_0^2 values equal to unit within their fit errors. The overall fit quality was however lower with respect to the O_2-activated Cu-SSZ-13 case, as reflected by the higher, although still satisfactory, R-factor values.

In particular, starting with the *8r1Al* model, the two coordination shell observed in the experimental spectrum were well reproduced employing only two Cu–O_{fw} and one Cu–T SS paths, with additional contribution in the high-R region from the remaining atoms in the *8r*. The corresponding bond distances from the cation are only slightly varied with respect to the DFT-optimized geometry, and adjusted to ~ 1.94 Å and ~ 2.71 Å for the O_{fw} and T coordination shells, respectively. However, as it can be noted in Table 3, the DW parameters for the two sets of paths were optimized to higher values with respect to the O_2-activated Cu-SSZ-13 case. These are still physically meaningful values, and the paths contribution to the two maxima of the experimental $|FT\{k^2\chi(k)\}|$ curve can be clearly identified (see Fig. 8b,c). Nevertheless, the higher DW values observed are clearly symptomatic of an increased structural disorder in the local environment of Cu(I) sites formed upon He-activation, whereas the thermal contribution to DW factors is unvaried with respect to the O_2-activated case, having collected the two spectra at the same temperature of 400 °C.

Further insights can be obtained by analyzing the result of the EXAFS fit performed according to the *d6r1Al* model. Here, the presence of an additional parameter in the fit model (radial shift of the two additional O'$_{(fw)}$ atoms at the average Cu–O'$_{(fw)}$ distance ~ 2.51 Å from DFT, see Table 1) ensured a moderate decrease in the R-factor value. A reduction of the DW values for all the included coordination shells was also observed with respect to the fit performed using the *8r1Al* model, although DW factors still significantly higher with respect to the O_2-activated material were found. Nevertheless, the best fit is obtained in correspondence of a pronounced contraction of the Cu–T distance, with $\Delta R_T \sim -0.16$ Å from the DFT values. This distortion is less critical with respect to what was obtained using the *d6r2Al#1* model to fit the spectrum of the O_2-activated sample ($\Delta R_{O'(fw)} \sim +0.24$ Å) but severe enough to suggest a partial inability of this model to reproduce by itself the experimental spectrum.

Table 3 Best-fit parameters optimized by EXAFS fits of the k^2-weighted spectrum of He-activated Cu-SSZ-13 (data collection at 400 °C), employing as starting guess DFT-optimized geometries for Cu(I) sites in the *8r* and *d6r* units of the zeolite framework, *i.e.* the *8r1Al* and *d6r1Al* models. The fit was performed in R-space, in the range (1.0 – 3.2) Å, employing the *k*-range (2.4 – 12.4) Å^{-1} for the FT, resulting in a maximum number of independent parameters equal to $N_{ind} = 2\Delta k \Delta R/\pi = 14$.

Best fit parameters for He-activated Cu-SSZ-13 - Cu(I) sites		
Optimized parameters	*8r1Al*	*d6r1Al*
S_0^2	1.1 ± 0.1	0.9 ± 0.1
ΔE (eV)	– 3 ± 1	– 5 ± 1
R-factor	0.01510	0.01073
N_{par}	8	9
$<R_{O(fw)}>$ (Å)	1.94 ± 0.01	1.92 ± 0.01
$\sigma^2_{O(fw)}$ (Å^2)	0.011 ± 0.002	0.006 ± 0.002
$N_{O(fw)}$	2	2
$<R_{O'(fw)}>$ (Å)	–	2.55 ± 0.05
$\sigma^2_{O'(fw)}$ (Å^2)	–	0.006 ± 0.002
$N_{O'(fw)}$	–	2
$<R_T>$ (Å)	2.71 ± 0.02	2.63 ± 0.04
σ^2_T (Å^2)	0.015	0.012 ± 0.002
N_T	1	2
α_{fw}	0.00 ± 0.01	0.01 ± 0.01
σ^2_{fw} (Å^2)	0.008 ± 0.003	0.008 ± 0.003
N_{fw}	4	6

In addition, the radial shift parameters for the $R_{O'(fw)}$ and T coordination shells are affected by a very high mutual correlation: $\Delta R_{O'(fw)}$ & $\Delta R_T \rightarrow 0.96$. As it can be observed in Fig. 8f, the respective SS paths are adjusted in an almost perfect antiphase, even though in this case the residual signal slightly differs from the Cu–T SS path refined for the *8r1Al* model. Hence, the fit routine is not just trying to restore the local environment of the *8r1Al* model, but likely bringing up a secondary contribution from the *d6r1Al* geometry. Not surprisingly, it was impossible to refine two independent structural components from both models, due to the limited "structural contrast" between the Cu(I) local geometries in *8r* and *d6r*, resulting in correlations > 0.9 between all the structural parameters involved. Finally, it is worth to note that the *d6r1Al* model closely resembles the *d6r2Al#1* Cu(II) configuration in terms of Cu nearest neighbours, upon replacement of one out of two Al atoms by a Si one in the T-site of the *d6r* ring (undistinguishable by EXAFS). Hence, the

secondary contribution overlapped to the major *8r1Al* component could also be assigned to difficultly reducible Cu(II) sites in the *d6r*. This possibility is corroborated by the already mentioned work by Mossin *et al.*[18], where the residual EPR signal from Cu-SSZ-13 dehydrated at 250 °C in He-flow has been related to the persistence of two well-defined EPR-active Cu(II) sites in the *d6r*, each accounting for ~ 9% of total Cu.

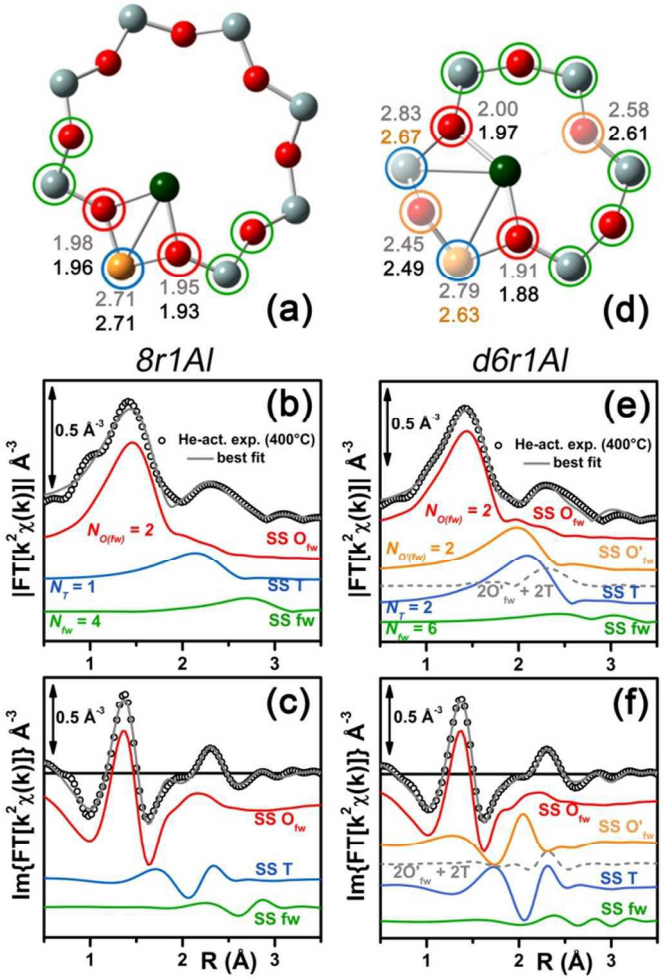

Fig. 8. (a),(d) Representation of the DFT-optimized (a) *8r1Al* and (d) *d6r1Al* geometries: atom colour code: Cu, green; O, red; Al, gold, Si, gray. Coloured circles highlight the different shells neighbouring atoms included in the fitting model. Starting DFT-optimized bond distances from the Cu absorber for each atom are reported in grey, while the correspondent values refined by EXAFS fitting are shown in black (distances are indicated in Å). (b),(c) Comparison between experimental EXAFS spectrum of the He-activated Cu-SSZ-13 catalyst and corresponding best fit performed from the *8r1Al* model; both modulus and imaginary parts of the FT are shown in part (b) and (c) respectively, together with the different SS paths contributions to the total signal, with the same colour code employed in part (a) and vertically translated for the sake of clarity. (f),(g) The same as parts (b),(c) but using the *d6r1Al* model as an input for the fit. Gray dashed lines indicate the residual signal after summing the O'fw and T contributions. For quantitative values of the parameters optimized in the two fits, see Table 3.

In conclusion, EXAFS analysis of He-activated Cu-SSZ-13 indicates the *8r1Al* model as most reliable average configuration. However, the fitting results also pointed out a higher structural disorder with respect to what observed for the O_2-activated sample, in concomitance to the probable presence of an additional minor contribution, either from "bare" Cu(I) sites in *d6r*, which arrange in a not-equivalent coordination environment, or from residual, difficulty-reducible Cu(II) species which presence is confirmed by HERFD XANES (see below).

DFT-assisted XANES and XES simulations for O_2-activated and He-activated Cu-SSZ-13

Along with the EXAFS fitting, calculations of the XANES and XES spectra for all the obtained DFT models were performed in order to complement the analysis. Since the features of the XANES spectra, recorded using conventional transmission setup are rather broad and not always clearly distinguishable, we will use HERFD XANES data with much more pronounced peaks for the comparison with theory. These spectra were collected in sample environment conditions analogous to the corresponding conventional XANES and therefore are fully equivalent to them.

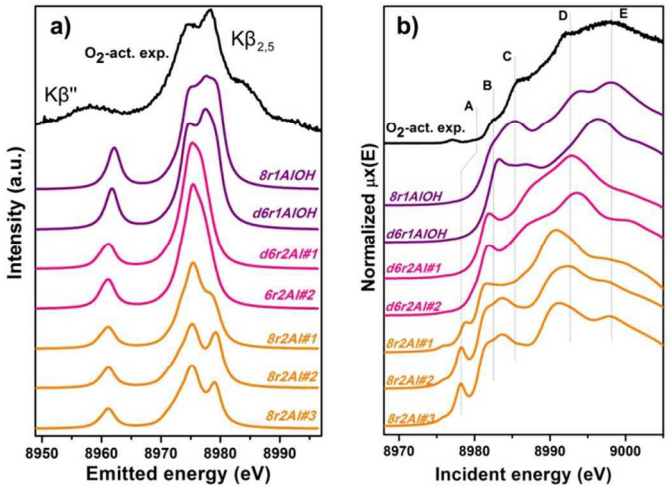

Fig. 9. Experimental XES (a) and HERFD XANES (b) spectra of O_2-activated Cu-SSZ-13 together with the simulated curves for different DFT models for Cu(II) sites presented in Fig. 5. Spectra are shifted along the vertical axis for the sake of clarity.

Fig. 9a shows the results of the XES simulations for the trial structures of Cu(II). Simulated spectra are divided into three groups: those that contain the extra-ligand OH group (purple), those with 2 Al atoms in the *d6r* (pink) and finally those with 2 Al atoms in the *8r* (orange). Similarly to EXAFS, XES simulations support the OH-like structures, since only in these cases it is possible to reproduce the double-peaked Kβ$_{2,5}$ line as it is present in the experiment. An interesting observation is that all the simulations fail to reproduce correctly the separation between Kβ$_{2,5}$ and Kβ" emission lines. Similar underestimation of this distance in the calculated XES of various Cu model compounds was reported recently by Vegelius *et al.*[69] That might indicate a systematic error in the treatment of ligand 2s orbitals by the chosen theoretical approaches, since that is the main origin of Kβ" satellite intensity.

Each of the three groups of XANES spectra (Fig. 9b) has its own characteristic features. In particular, all *8r2Al* structures (orange lines) exhibit a distinct peak in the lower energy region (feature **A**), that is completely absent in the other simulated

spectra. In the experimental data, one can only observe a very minor contribution from this transition. Along with the general mismatch in the shape of the spectra, this allows to rule out these low-coordinated configurations as the major species for O_2 activated Cu-SSZ-13. Disagreement with the experiment in the shape of the main maxima (peaks **D** and **E**) does not favor structures with 2 Al atoms in the *d6r* (pink curves) as well. Best results in terms of peak positions were obtained for the *8r1AlOH* model, in agreement with the EXAFS fitting results reported above. Notably, the spectrum of the *d6r1AlOH* structure provided a significantly worse reproduction of the experimental curve, demonstrating a higher sensitivity of XANES compared to EXAFS and XES, where the two OH-like models in *d6r* and *8r* yielded very similar results.

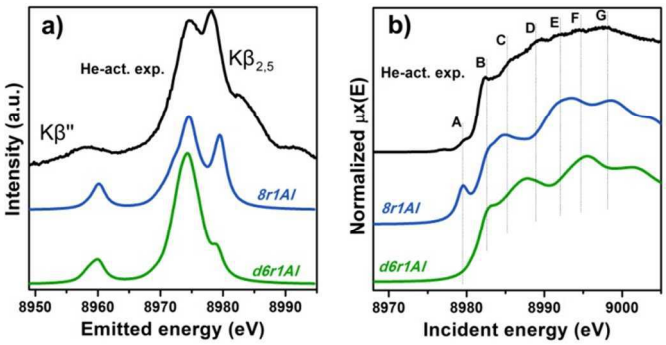

Fig. 10. Experimental XES (a) and HERFD XANES (b) spectra of He activated Cu-SSZ-13 together with the simulated curves for different DFT models for Cu(I) sites presented in Fig. 5. Spectra are shifted along the vertical axis for the sake of clarity.

However, it is worth noting that for a relatively inhomogeneous system like Cu-SSZ-13 the enhanced sensitivity of XANES can also be a disadvantage, since all the Cu species present in the sample contribute in a different way to the signal. Hence, is not surprising that none of the simulations is in line-to-line agreement with the experiment. This problem should have been faced by Deka *et al.*[31] as well, who have reported to the best of our knowledge the only Cu K-edge XANES simulation of the activated Cu-SSZ-13 up to now. Nonetheless, the simulation has allowed them to demonstrate that copper shifts towards the framework rather than staying in the middle of the cavity. The problem of inhomogeneity is even more evident looking at the XES and XANES simulations of the spectra collected for the He-activated catalyst (Fig. 10). EXAFS conclusion about a much higher degree of disorder in the local environment of copper is confirmed by rather strong discrepancies between experiment and theory. Nonetheless, XES simulations (Fig. 10a) suggest that *8r* structure is more favorable, since it yields the double-peaked $K\beta_{2,5}$, unlike the competing *d6r* model. The large number of peaks present in the experimental HERFD XANES suggests that several not-negligible species are present in the sample at these activation conditions, in agreement with EPR results of Mossin *et al.*[18] Interestingly, peaks in the calculated spectra of the two trial structures are often in antiphase, which might explain a broad main maximum with several weak oscillations (features **D**–**G**), visible in the experiment. It indicates that both of these two species are likely to exist in the material, *8r1Al* being more abundant since only this structure can be the origin of the pre-edge peak **A**, whose intensity in the experiment increased significantly compared to the case of O_2-activation. Remarkably, the 1s → 3d peak is still present in the experimental data, suggesting a residual contribution of oxidized Cu (II) species as well. However, their amount should be rather low, since the peak is so weak that it is visible only in the high-resolution mode due to a very low background, and completely absent in the conventional XANES.

Summing up it is possible to conclude that XES and XANES data support the findings of DFT and EXAFS. The performed simulations suggest that copper is more likely to dwell in the larger 8-member ring cavities than in smaller 6-member rings. Likewise, formation of $[CuOH]^+$ complexes is favored in case of the activation in O_2 compared to the alternative of "bare" Cu^{2+} ions in the rings that contain two aluminum atoms. Despite the fact that the afore mentioned presence of many rather different Cu species in the material worsens the agreement of the simulated XES and XANES spectra with the experiment, these methods proved to be an invaluable complement for EXAFS and DFT data, which is particularly important when studying such complex systems like Cu-SSZ-13.

Conclusions and perspectives

The dehydration process in Cu-SSZ-13 catalyst has been monitored by XAS and FTIR spectroscopy in the RT – 400 °C temperature range. Depending on the adopted thermal treatments, namely O_2-activation and He-activation, different Cu species have been found to be formed. Data analysis revealed that dehydration process of Cu cations is substantially completed at 250 °C, with the formation of dehydrated $[CuOH]^+$ species strongly interacting with the zeolite framework. These species are maintained even at higher temperature only if a certain amount of O_2 is present in the gas feed. Otherwise, they undergo virtually total "self-reduction" as a consequence of an OH extra-ligand loss. The reversibility of the process has been verified at 400 °C, demonstrating the high Cu(II)/Cu(I) redox capability. On the basis of these novel findings, the dehydration process and the effect of different activation conditions on the Cu-speciation in the Cu-SSZ-13 catalyst can be revised according to Scheme 1.

We tested by detailed EXAFS analysis in combination with XANES/XES simulations different DFT-optimized structures, and by comparison with the experimental data we found that the majority of dehydrated Cu species are hosted in a close proximity of 1 Al sites, preferentially in *8r* units of the SSZ-13 matrix. In particular, our results strongly support tri-coordinated $[CuOH]^+$ species as dominant structural component upon O_2-activation; conversely, bi-coordinated bare Cu^+ cations in *8r* units have been found to represent the most abundant configuration upon He-activation. Other configurations, if present, are supposed to occur in percentages small enough to hamper the deconvolution of their contributions from the total XAS/XES signals, inherently averaged on all the Cu-sites. Nonetheless, the formation of a significant fraction of dimeric oxo-Cu species, *i.e.* Cu_xO_y (per mole Cu, $x \geq 2$, $y \geq 1$), seems to

be very unlikely. This reinforces the idea that Cu-SSZ-13 catalyst mainly contains monomeric Cu species, in the form of redox-active $[CuOH]^+$ complexes, which are thought to play a key role in the NH_3-SCR mechanism. The present findings pave the way to the future understanding of the nature of the catalytic centres in working conditions. On one side, they provide the starting structures that reactants will found when fed on the activated catalyst. On the other hand, the high stability of both Cu^{2+} and Cu^+ species identified in the present work as dominant structural components upon O_2-activation and He-activation, namely $[CuOH]^+$ and bare Cu^+ cations, strongly suggests that these moieties play as key intermediates along the SCR catalytic cycle. Future experiments in *operando* conditions are however required to confirm this hypothesis and to unravel the other species involved in the reaction mechanism.

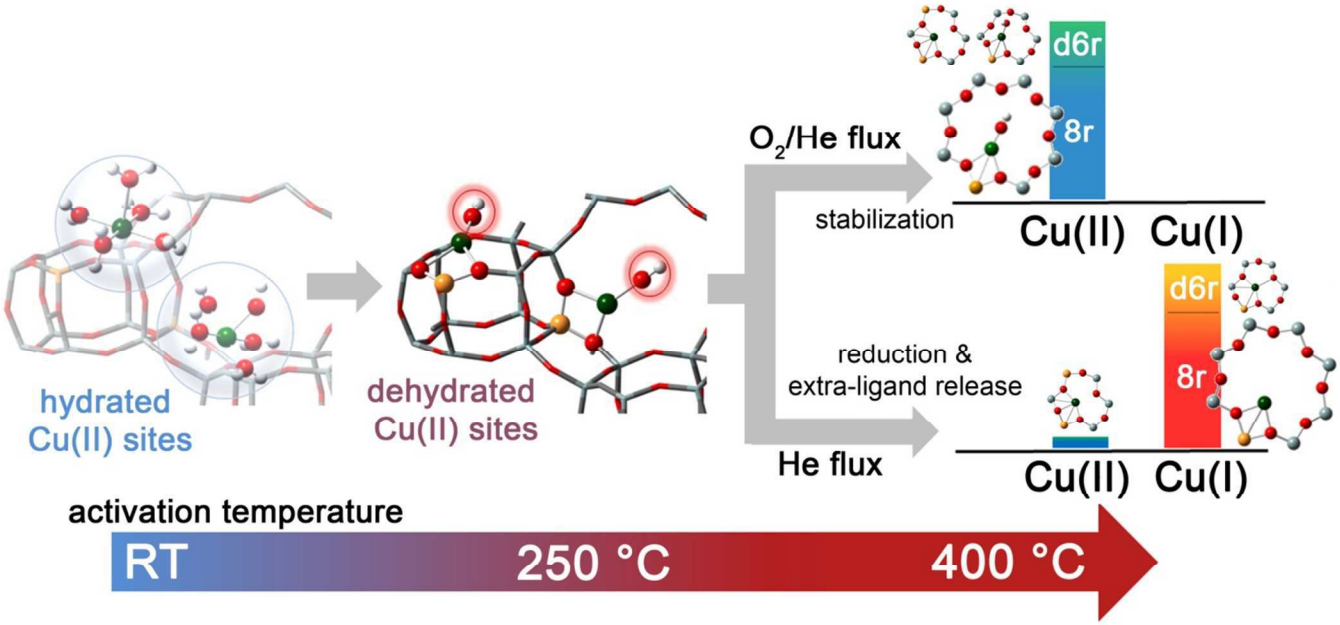

Scheme 1. Schematic representation of Cu-speciation in Cu-SSZ-13 catalyst as a function of the dehydration temperature and conditions. In the O_2-activated Cu-SSZ-13 we found virtually no traces of Cu(I) within the experimental incertitude of the employed techniques. Conversely, the presence of a minor fraction (around 10%) of Cu(II) in the He-activated sample was detectable in HERFD XANES. The larger geometries depicted in the right side of the scheme are the dominant structural components identified by XAS, XES and FTIR in the Cu-SSZ-13 sample investigated in the present work.

Acknowledgements

This work has been supported by "Progetti di Ricerca di Ateneo-Compagnia di San Paolo-2011- Linea 1", ORTO11RRT5 project. CL, KAL and AVS thank the support from the Mega-grant of the Russian Federation Government to support scientific research at Southern Federal University, No.14.Y26.31.0001.

The authors would like to thanks G. Agostini and O. Mathon, and P. Glatzel and E. Gallo for their helping during beamtime on BM23 and ID26. We are also grateful to P. Vennestrøm for useful support on the computational analysis.

Notes and references

[a] Department of Chemistry and INSTM Reference Center, University of Turin, via P. Giuria 7, 10125 Turin, Italy

[b] NIS Centre of Excellence, University of Turin, Italy

[c] Haldor Topsøe A/S, Nymøllevej 55, 2800 Kgs. Lyngby, Denmark

[d] CrisDI center of crystallography, University of Turin, Italy

[e] Southern Federal University, Zorge street 5, 344090 Rostov-on-Don, Russia

Electronic Supplementary Information (ESI) available: Experimental section (sample description, in situ FTIR spectroscopy, synchrotron characterization, DFT-based analysis of XAS and XES data); XAS of hydrated Cu-SSZ-13; reversibility of the Cu(I) ↔ Cu(II) redox chemistry and extra-ligand loss process upon high-temperature gas-flow switching; full report on DFT-optimized geometries; full report on EXAFS fitting results on O_2-activated Cu-SSZ-13; EXAFS spectra for a low Cu-loading Cu-SSZ-13 sample after O_2-activation at 400 °C. See DOI: 10.1039/b000000x/

1. P. Granger and V. I. Parvulescu, *Chem. Rev.*, 2011, **111**, 3155-3207.
2. S. Brandenberger, O. Krocher, A. Tissler and R. Althoff, *Catal. Rev.*, 2008, **50**, 492-531.
3. U. Deka, I. Lezcano-Gonzalez, B. M. Weckhuysen and A. M. Beale, *ACS Catal.*, 2013, **3**, 413-427.
4. F. Gao, J. Kwak, J. Szanyi and C. F. Peden, *Top. Catal.*, 2013, **56**, 1441-1459.
5. C. H. F. Peden, J. H. Kwak, S. D. Burton, R. G. Tonkyn, D. H. Kim, J.-H. Lee, H.-W. Jen, G. Cavataio, Y. Cheng and C. K. Lambert, *Catal. Today.*, 2011, **184**, 245-251.
6. V. I. Parvulescu, P. Grange and B. Delmon, *Catal. Today*, 1998, **46**, 233-316.
7. J. H. Kwak, J. H. Lee, S. D. Burton, A. S. Lipton, C. H. F. Peden and J. Szanyi, *Angew. Chem. Int. Ed.*, 2013, 10169–10173.
8. J. H. Kwak, D. Tran, S. D. Burton, J. Szanyi, J. H. Lee and C. H. F. Peden, *J. Catal.*, 2012, **287**, 203-209.
9. J. H. Kwak, D. Tran, J. Szanyi, C. H. F. Peden and J. H. Lee, *Catal. Lett.*, 2012, **142**, 295-301.

10. J. H. Kwak, H. Y. Zhu, J. H. Lee, C. H. F. Peden and J. Szanyi, *Chem. Comm.*, 2012, **48**, 4758-4760.
11. F. Gao, E. D. Walter, E. M. Karp, J. Luo, R. G. Tonkyn, J. H. Kwak, J. Szanyi and C. H. F. Peden, *J. Catal.*, 2013, **300**, 20-29.
12. J. H. Kwak, R. G. Tonkyn, D. H. Kim, J. Szanyi and C. H. F. Peden, *J. Catal.*, 2010, **275**, 187-190.
13. D. W. Fickel, J. M. Fedeyko and R. F. Lobo, *J. Phys. Chem. C*, 2010, **114**, 1633-1640.
14. S. T. Korhonen, D. W. Fickel, R. F. Lobo, B. M. Weckhuysen and A. M. Beale, *Chem. Comm.*, 2011, **47**, 800-802.
15. F. Giordanino, P. N. R. Vennestrom, L. F. Lundegaard, F. N. Stappen, S. L. Mossin, P. Beato, S. Bordiga and C. Lamberti, *Dalton Trans.*, 2013, **42**, 12741-12761.
16. C. Andersen, M. Bremholm, P. Vennestrøm, A. Blichfeld, L. Lundegaard and I. B., *IUCrJ*, in press, doi:10.1107/S2052252514020181.
17. F. Giordanino, E. Borfecchia, K. A. Lomachenko, A. Lazzarini, G. Agostini, E. Gallo, A. V. Soldatov, P. Beato, S. Bordiga and C. Lamberti, *J. Phys. Chem. Lett.*, 2014, **5**, 1552-1559.
18. S. Mossin, A. Godiksen, F. Stappen, P. Vennestrøm, F. Giordanino, L. Lundegaard and S. Rasmussen, *J. Phys. Chem. C*, 2014, **118**, 23126-23138.
19. A. A. Verma, S. A. Bates, T. Anggara, C. Paolucci, A. A. Parekh, K. Kamasamudram, A. Yezerets, J. T. Miller, W. N. Delgass, W. F. Schneider and F. H. Ribeiro, *J. Catal.*, 2014, **312**, 179-190.
20. J. A. van Bokhoven, T. L. Lee, M. Drakopoulos, C. Lamberti, S. Thiess and J. Zegenhagen, *Nat. Mater.*, 2008, **7**, 551-555.
21. F. Goltl, R. E. Bulo, J. Hafner and P. Sautet, *J. Phys. Chem. Lett.*, 2013, **4**, 2244-2249.
22. J. S. McEwen, T. Anggara, W. F. Schneider, V. F. Kispersky, J. T. Miller, W. N. Delgass and F. H. Ribeiro, *Catal. Today*, 2012, **184**, 129-144.
23. F. Gao, E. D. Walter, M. Kollar, Y. Wang, J. Szanyi and C. H. F. Peden, *J. Catal.*, 2014, **319**, 1-14.
24. C. Paolucci, A. A. Verma, S. A. Bates, V. F. Kispersky, J. T. Miller, R. Gounder, W. N. Delgass, F. H. Ribeiro and W. F. Schneider, *Angew. Chem. Int. Ed.*, in press, doi: 10.1002/anie.201407030.
25. C. Lamberti, E. Groppo, G. Spoto, S. Bordiga and A. Zecchina, *Adv Catal*, 2007, **51**, 1-74.
26. C. Lamberti, A. Zecchina, E. Groppo and S. Bordiga, *Chem. Soc. Rev.*, 2010, **39**, 4951-5001.
27. S. Bordiga, E. Groppo, G. Agostini, J. A. van Bokhoven and C. Lamberti, *Chem. Rev.*, 2013, **113**, 1736-1850.
28. L. Mino, G. Agostini, E. Borfecchia, D. Gianolio, A. Piovano, E. Gallo and C. Lamberti, *J. Phys. D-Appl. Phys.*, 2013, **46**, 423001.
29. C. Garino, E. Borfecchia, R. Gobetto, L. Salassa, J. A. van Bokhoven and C. Lamberti, *Coord. Chem. Rev.*, 2014, **277–278** 130-186.
30. V. F. Kispersky, A. J. Kropf, F. H. Ribeiro and J. T. Miller, *Phys. Chem. Chem. Phys.*, 2012, **14**, 2229-2238.
31. U. Deka, A. Juhin, E. A. Eilertsen, H. Emerich, M. A. Green, S. T. Korhonen, B. M. Weckhuysen and A. M. Beale, *J. Phys. Chem. C*, 2012, **116**, 4809-4818.
32. J. H. Kwak, T. Varga, C. H. F. Peden, F. Gao, J. C. Hanson and J. Szanyi, *J. Catal.*, 2014, **314**, 83-93.
33. P. Glatzel and U. Bergmann, *Coord. Chem. Rev.*, 2005, **249**, 65-95.
34. G. Smolentsev, A. V. Soldatov, J. Messinger, K. Merz, T. Weyhermuller, U. Bergmann, Y. Pushkar, J. Yano, V. K. Yachandra and P. Glatzel, *J. Am. Chem. Soc.*, 2009, **131**, 13161-13167.
35. J. Singh, C. Lamberti and J. A. van Bokhoven, *Chem. Soc. Rev.*, 2010, **39**, 4754-4766.
36. A. Boubnov, H. W. P. Carvalho, D. E. Doronkin, T. Günter, E. Gallo, A. J. Atkins, C. R. Jacob and J.-D. Grunwaldt, *J. Am. Chem. Soc.*, 2014, **137**, 13006–13015.
37. S. Bordiga, L. Regli, C. Lamberti, A. Zecchina, M. Jorgen and K. P. Lillerud, *J. Phys. Chem. B*, 2005, **109**, 7724-7732.
38. K. Hadjiivanov, J. Saussey, J. L. Freysz and J. C. Lavalley, *Catal. Lett.*, 1998, **52**, 103-108.
39. S. Bordiga, L. Regli, D. Cocina, C. Lamberti, M. Bjorgen and K. P. Lillerud, *J. Phys. Chem. B*, 2005, **109**, 2779-2784.
40. L. Marchese, J. Chen, J. M. Thomas, S. Coluccia and A. Zecchina, *J. Phys. Chem.*, 1994, **98**, 13350-13356.
41. E. Ito, Y. J. Mergler, B. E. Nieuwenhuys, H. P. A. Calis, H. van Bekkum and C. M. van den Bleek, *J. Chem.Soc., Farad.Trans.*, 1996, **92**, 1799-1806.
42. M. Iwasaki and H. Shinjoh, *J. Catal.*, 2010, **273**, 29-38.
43. C. Lamberti, S. Bordiga, M. Salvalaggio, G. Spoto, A. Zecchina, F. Geobaldo, G. Vlaic and M. Bellatreccia, *J. Phys. Chem. B*, 1997, **101**, 344-360.
44. M. H. Groothaert, J. A. van Bokhoven, A. A. Battiston, B. M. Weckhuysen and R. A. Schoonheydt, *J. Am. Chem. Soc.*, 2003, **125**, 7629-7640.
45. E. M. C. Alayon, M. Nachtegaal, A. Bodi and J. A. van Bokhoven, *ACS Catal.*, 2014, **4**, 16-22.
46. S. C. Larsen, A. Aylor, A. T. Bell and J. A. Reimer, *J. Phys. Chem.*, 1994, **98**, 11533-11540.
47. G. T. Palomino, S. Bordiga, A. Zecchina, G. L. Marra and C. Lamberti, *J. Phys. Chem. B*, 2000, **104**, 8641-8651.
48. F. X. Llabrés i Xamena, P. Fisicaro, G. Berlier, A. Zecchina, G. T. Palomino, C. Prestipino, S. Bordiga, E. Giamello and C. Lamberti, *J. Phys. Chem. B*, 2003, **107**, 7036-7044.
49. P. N. R. Vennestrøm, T. V. W. Janssens, A. Kustov, M. Grill, A. Puig-Molina, L. F. Lundegaard, R. R. Tiruvalam, P. Concepción and A. Corma, *J. Catal.*, 2014, **309**, 477-490.
50. L. S. Kau, D. J. Spirasolomon, J. E. Pennerhahn, K. O. Hodgson and E. I. Solomon, *J. Am. Chem. Soc.*, 1987, **109**, 6433-6442.
51. M. Sano, S. Komorita and H. Yamatera, *Inorg. Chem.*, 1992, **31**, 459-463.
52. P. S. Salmon, G. W. Neilson and J. E. Enderby, *J. Phys. C.*, 1988, **21**, 1335-1349.
53. M. Benfatto, P. D'Angelo, S. Della Longa and N. V. Pavel, *Phys. Rev. B*, 2002, **65**, 174205.
54. P. Frank, M. Benfatto, R. K. Szilagyi, P. D'Angelo, S. Della Longa and K. O. Hodgson, *Inorg. Chem.*, 2005, **44**, 1922-1933.
55. J. Chaboy, A. Munoz-Paez, P. J. Merkling and E. S. Marcos, *J. Chem. Phys.*, 2006, **124**.
56. G. T. Palomino, P. Fisicaro, S. Bordiga, A. Zecchina, E. Giamello and C. Lamberti, *J. Phys. Chem. B*, 2000, **104**, 4064-4073.
57. K. Kervinen, P. C. A. Bruijnincx, A. M. Beale, J. G. Mesu, G. van Koten, R. Gebbink and B. M. Weckhuysen, *J. Am. Chem. Soc.*, 2006, **128**, 3208-3217.

58. J. M. Tranquada, S. M. Heald and A. R. Moodenbaugh, *Phys. Rev. B*, 1987, **36**, 5263-5274.
59. C. Prestipino, G. Berlier, F. Xamena, G. Spoto, S. Bordiga, A. Zecchina, G. T. Palomino, T. Yamamoto and C. Lamberti, *Chem. Phys. Lett.*, 2002, **363**, 389-396.
60. L. S. Kau, K. O. Hodgson and E. I. Solomon, *J. Am. Chem. Soc.*, 1989, **111**, 7103-7109.
61. M. Occhiuzzi, G. Fierro, G. Ferraris and G. Moretti, *Chem. Mater.*, 2012, **24**, 2022-2031.
62. W. Loewenstein, *Am. Mineral.*, 1954, **39**, 92-96.
63. H. Hamada, N. Matsubayashi, H. Shimada, Y. Kintaichi, T. Ito and A. Nishijima, *Catal. Lett.*, 1990, **5**, 189-196.
64. W. Grunert, N. W. Hayes, R. W. Joyner, E. S. Shpiro, M. R. H. Siddiqui and G. N. Baeva, *J. Phys. Chem.*, 1994, **98**, 10832-10846.
65. A. B. Ene, M. Bauer, T. Archipov and E. Roduner, *Phys. Chem. Chem. Phys.*, 2010, **12**, 6520-6531.
66. F. Boscherini, C. Lamberti, S. Pascarelli, C. Rigo and S. Mobilio, *Phys. Rev. B*, 1998, **58**, 10745-10753.
67. C. Lamberti, *Surf. Sci. Rep.*, 2004, **53**, 1-197.
68. E. Borfecchia, S. Maurelli, D. Gianolio, E. Groppo, M. Chiesa, F. Bonino and C. Lamberti, *J. Phys. Chem. C*, 2012, **116**, 19839-19850.
69. J. R. Vegelius, K. O. Kvashnina, M. Klintenberg, I. L. Soroka and S. M. Butorin, *J. Anal. At. Spectrom.*, 2012, **27**, 1882-1888.

Table of contents entry

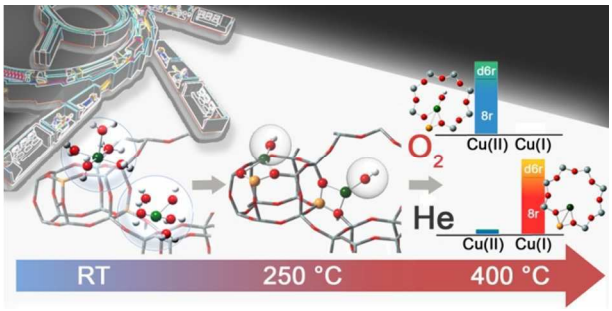

X-ray absorption and emission spectroscopy, FTIR and DFT unravel the major Cu-species in the activated Cu-SSZ-13 catalyst for NH_3-SCR.